Role of oxide-derived Cu on the initial elementary reaction intermediate during catalytic CO 2 reduction

Zhiwen Jiang, Carine Clavaguéra, Sergey Denisov, Jun Ma, Mehran Mostafavi

Role of oxide-derived Cu on the initial elementary reaction intermediate during catalytic CO_2 reduction

Zhiwen Jiang, [†,‡] Carine Clavaguéra,[‡] Sergey A. Denisov,[‡] Jun Ma,[†*] Mehran Mostafavi[‡*]

[†] *School of Nuclear Science and Technology, University of Science and Technology of China, Hefei, Anhui 230026, China.*

[‡] *Université Paris-Saclay, CNRS, Institute de Chimie Physique, UMR8000, 91405, Orsay, France.*

ABSTRACT: The catalytic role of oxide-derived Cu (OD-Cu) in promoting CO_2 reduction (CO_2R) to C_{2+} products has been appreciated for decades. However, the dynamic evolution of the surface oxidation states, together with its real correlation to the binding of reaction intermediates, remains unclear due to technical challenges. Here, we show the time-resolved spectroscopic signatures of key OD-Cu-$CO_2^{\bullet-}$ intermediates during catalytic CO_2 reduction through one electron transfer from nanoseconds to seconds time scale. We generate the initial intermediate $CO_2^{\bullet-}$ radicals in the bulk solution and monitor the interfacial reaction kinetics with well-defined OD-Cu (Cu(0), Cu(I), and Cu(II)) nanoparticles. Combined with molecular simulations, transient absorption profiles analysis reveals that Cu(I) induced a faster $CO_2^{\bullet-}$ radical coupling reaction than Cu(0), whereas Cu(II) is only reduced to Cu(I) by $CO_2^{\bullet-}$ radical. Furthermore, the newly developed multi-step cumulative pulse methodology uncovered the transition in chemical states of mixed OD-Cu during radical coupling reactions. This pulse radiolysis study provides compelling evidence for the beneficial role of subsurface oxide in early-time catalytic CO_2 transformation.

1. INTRODUCTION

Carbon dioxide (CO_2) mitigation is one of the most important challenges of our time. One promising avenue has been converting this gas by renewable energy into valuable chemicals and fuels that can be subsequently used as feedstock for the chemical industry or as energy storage technology. Copper stands out as the singular catalyst with an exceptional ability to generate high-value multi-carbon C_{2+} products during CO_2 reduction in aqueous media[1,2], especially when the electrode is nanostructured and derived from an oxide[1-3]. The involvement of oxidized Cu-based catalysts has also been appreciated in many other CO_2 conversion routes, such as photolytic, radiolytic, and plasma strategies. In most cases, it leads to an increased catalytic performance[4-6]. Such widespread recognition makes oxide-derived copper (OD-Cu) essential in sustainable CO_2 transformations to achieve carbon neutrality. Over the decades, extensive experimental and theoretical studies have been conducted to address the critical roles of OD-Cu in initial CO_2 activation and subsequent C–C coupling reactions; however, up to now, the mechanistic understanding remains debated.

The controversial points are rooted in the simultaneous occurrence of oxidation state variations and surface restructuring during catalytic CO_2 reduction[7,8]. The interplay of these two elementary processes makes the identification of active sites considerably complex. Atomic rearrangement readily leads to macroscopical structural changes of OD-Cu in size, shape, facets, grain boundary, and element distribution, thus affecting the CO_2 reduction framework[9-11]. Recent advances in spatial-resolved operando techniques make it possible to observe what has only been theoretically presumed to occur. The studies show that facet and nanograins rearrangements, contribute to the C–C coupling reaction and higher C_{2+} selectivity[12-17]. In contrast to spatial evolution, the direct observation of the swift transformations of oxidation state in real-time during catalytic CO_2 reduction has been another long-standing experimental challenge. The oxidation states are also likely to vary due to the complex nature of Cu species coordinated with reactant intermediates[2, 12, 13]. For example, Cu(I) readily undergoes the dismutation to generate Cu(II) and Cu(0). Applying an external potential makes it susceptible to being reduced to Cu(0) or oxidized to Cu(II) by elusive O_2 and other short-lived oxidizing species[14, 15]. The operational factors, such as cathodic voltage, localized pH, and intermediates, can reduce or reoxidize OD-Cu rapidly.

Previous attempts led to different interpretations concerning the precise oxidation states of Cu as active sites for promoting catalytic CO_2 reduction[8, 16-19]. Some studies demonstrated that high selectivity to C_{2+} products could also occur in the OD-Cu with completely reduced surfaces. For example, operando grazing incidence X-ray studies by Drisdell *et al.*[20] revealed that the surface oxide layer on polycrystalline Cu electrodes was fully reduced before onset potential. Cu(0) surface could be well maintained at the metallic state across the potentials relevant to the CO_2R. In contrast, Roldan *et al.*[18] suggested that OD-Cu were resistant to reduction, and Cu(I) species remained on the surface during the reaction. The presence of Cu(I) species, as observed by operando X-ray absorption spectroscopy, is more relevant to catalytic performance rather than the roughness of catalysts. An electrochemical study of oxygen plasmas-modified dendritic Cu catalysts found that C_{2+}

product selectivity trends can be exclusively assigned to their morphology and the contribution from exposed regions of the respective underlying supports (Ag or Pt)[17]. Such discrepancies have posed significant challenges in the conclusive contribution of oxidation states of OD-Cu and thus have greatly hindered the rational design of catalysts for better performance. To date, most operando methods based on X-ray, infrared, or Raman spectroscopy are limited to subsecond time resolution, which have failed to reveal the key spectroscopic signature during the initial stages of CO_2RR. No detailed in situ or operando technique is available on the initial surface-bound intermediates to shed light on the ultrafast transformations in the chemical state of OD-Cu under CO_2RR conditions.

The recent development of electron pulse radiolysis coupled with optical spectroscopy made it feasible to measure the transient CO_2 reduction reactions at an unparalleled wide timescale from picoseconds[21-23] to microseconds[24-26]. Figure 1a shows the schematic of the picosecond pulse radiolysis system. A focused 8 MeV electron pulse with ~7 picosecond pulse width was used to ionize liquid water to produce the short-lived hydrated electron (e_{aq}^-) absorbing at 718 nm. Bulk $CO_2^{\bullet-}$ radicals can be formed in a quantitative yield via e_{aq}^- attachment to CO_2 within 10 ns, which is known as the initial intermediate during CO_2 reduction. Such rapid reaction excludes possible disturbing consequences, including electrolyte effects, competing reactions, and surface structure evolution or catalyst oxidation[27]. In the presence of synthetic nanoscale OD-Cu catalysts in CO_2-saturated solution, this method enables to elucidate of the electronic transitions of surface-bound intermediates via time-resolved spectroscopic signature, which is not accessible by existing subsecond operando techniques[28-30]. Besides, the simplicity of water radiolysis has often been described as "electrolysis without electrode". Based on the redox potential of $CO_2^{\bullet-}$ (−2.0 V) and e_{aq}^- (−2.7 V), the stability of oxidation states of OD-Cu can be estimated under a similar external potential. More importantly, each tunable high-energy pulse provides a known quantitative yield of electrons (μmol/J). For this reason, the precise manipulation of OD-Cu surfaces with gradient reduction levels becomes possible through the cumulative pulse. As a result, the transient spectroscopic method is well suited for the meticulous quantification of catalyst oxidation states in line with surface-bound intermediates dynamics.

Herein, we use the radiolytic reducing species to prepare various well-defined nanoscale OD-Cu (Cu(I), Cu(II), and their complex) via the reduction of Cu precursors. The formation of OD-Cu surface-bound $CO_2^{\bullet-}$ with the characteristic spectral band is identified by pulse radiolysis measurements and density functional theory (DFT) calculation. More importantly, we developed a multi-step cumulative pulse methodology to clarify the possible transition of OD-Cu in chemical states at the same moment that the reaction of surface-bound $CO_2^{\bullet-}$ radicals occurs.

2. EXPERIMENTAL SECTION

Chemicals. Copper(II) sulfate pentahydrate ($CuSO_4{\cdot}5H_2O$), Sodium formate (HCOONa), and cetyltrimethylammonium chloride (CTAC) were purchased from Sigma-Aldrich (Shanghai) Trading Co. Ltd. All chemicals were used as received. Ultrapure water with a resistivity of 18.2 MΩ cm was used in all experiments.

Synthesis of different nanoparticles. All nanoparticles (NPs) were synthesized by steady-state radiolytic methods. In a typical synthesis for Cu(I)-1 and Cu(I)-2 NPs, 2 mmol sodium formate and 0.5 mmol CTAC were added to 10 mL H_2O. Then, 10 mL copper(II) sulfate (1 mmol/L) solution was added to form homogeneous solutions. The solutions were saturated with CO_2 and sealed in a homemade cuvette. The cuvette was irradiated at a ^{60}Co gamma source (5.35×10^{13} Bq, located in the Université Paris-Saclay) at a dose rate of 2.2 kGy/h at ambient conditions. The dose rate was calibrated using the Fricke dosimeter. The resulting Cu(I) nanoparticle solution was directly used for pulse radiolysis experiments and absorption spectroscopy characterization.

For Cu(I)-3 NPs, the atmosphere was replaced with Ar during gamma irradiation. For Cu(II) NPs, the resulting Cu(I)-2 NPs solutions were heated under 60 °C for 12 h to oxidize Cu(I) NPs to Cu(II) NPs.

The Cu(0) NPs were prepared according to our previous report. In a typical synthesis for Cu nanoparticles, 2 mmol sodium formate, and 0.5 mmol CTAC were added to 10 mL H_2O. Then, 10 mL copper(II) sulfate (1 mmol/L) solution was added to form homogeneous solutions. The solutions were saturated with Ar and sealed in a homemade cuvette. The cuvette was irradiated at a ^{60}Co gamma source at a dose rate of 2.2 kGy/h at ambient conditions for 6.6 kGy. The resulting Cu nanoparticle solution was directly used for pulse radiolysis experiments and absorption spectroscopy characterization.

Characterization. UV-vis spectra were recorded on a UV-spectrophotometer (HEWLETT PACKARD 8453, HP) in the range from 190 to 800 nm. XPS analysis was performed on a Thermo Fisher Scientific ESCALAB 250Xi spectrometer using monochromatic Al Kα radiation (1486.6 eV; 150 W; 500 μm diameter of irradiated area).

Electrochemical Measurements. All the electrochemical experiments were carried out by a potentiostat (CS2350H, Wuhan Corrtest Instruments Corp., Ltd. China) with a three-electrode system including a working electrode, a counter electrode of Pt mesh, and a reference electrode of Ag/AgCl in a H-type cell. The carbon paper loaded with the catalyst was used as the work electrode. The catalyst ink was obtained by mixing 7 mg of as-synthesized catalyst and 50 μL of Nafion into a mixture containing 950 μL of ethanol, followed by 1 h sonication. The catalyst ink with a volume of 100 μL was deposited onto a precleaned carbon paper, which was dried at room temperature as a consequence of the loading concentration of 0.7 mg cm^{-2}. The electrolyte was 0.5 M $KHCO_3$ saturated with CO_2 or Ar. Linear sweep voltammetry (LSV) was recorded at the scanning rate of 5 mV s^{-1} with the potential window from −0.1 V to −1.5 V. The gas product was detected by gas chromatograph (GC, GC9790PLUS, Fuli Instruments, China) with a flame ionization detector (FID) and a thermal conductivity detector (TCD). All potentials in this work were converted to potentials versus reversible hydrogen electrode (RHE) according to the following equation: $E_{(vs.\ RHE)} = E_{(vs.\ Ag/AgCl)} + 0.197 + 0.059{\cdot}pH$.

Pulse radiolysis. Pulse radiolysis experiments were carried out employing the picosecond laser-triggered electron accel-

erator, ELYSE, coupled with a time-resolved absorption spectrophotometric detection system. Laser (260 nm) driven Cs_2Te photocathode allows the production of short electron pulses with a typical half width of 7 ps, a charge of ~ 6 nC, and an energy of ~ 7.8 MeV at a repetition rate of 10 Hz. During irradiation, metal nanoparticle solutions were contained in a homemade cell with a path length of 1 cm. The diameter of the electron beam was 3 mm, and the irradiated volume was less than 0.1 mL.

Absorption spectral measurements were performed using the white light from a homemade Xenon flash lamp. The light (48 mW/m^2) was focused on the sample parallel to the electron beam with a smaller diameter and then directed onto a flat field spectrograph (250IS, Chromex), which disperses the light on the entrance optics of a high dynamic range streak-camera (C-7700-01, HAMAMATSU) to obtain an image resolved in wavelength and time. The kinetic data and absorption spectra were extracted from three series of 200 resulting images. In this work, the transient spectra were measured from 290 to 720 nm at 1 µs, 10 µs, 20 µs, 100 µs, and 1 ms.

Computational Methods. The structures of the systems were optimized without constraint at the DFT level, using the PBE functional, the SDD pseudopotential with 19 valence-electrons treated explicitly for Cu atoms, and the def2-SVP basis set for carbon and oxygen atoms. In all the calculations, solvent effects were implicitly represented by a dielectric continuum model using the SMD method, and dispersion corrections were added to the functional used in the D3BJ framework[31]. The calculations on the Cu(0) NP with different numbers of atoms (38 and 50) were conducted as previously reported[43]. The Cu(II) NP was modeled by a $Cu_{38}O_{38}$ cluster whose starting structure was extracted from a previous DFT study[32]. The $Cu_{32}O_{15}$ model of the Cu(I) NP was built from the crystallographic structure[33]. To simulate oxygen loss, additional Cu(I) and Cu(II) calculations were performed with 4 oxygen atoms less than in the initial structure leading to the $Cu_{32}O_{11}$- $CO_2^{\bullet-}$ and the $Cu_{38}O_{34}$- $CO_2^{\bullet-}$ structures, respectively. The NPs were considered in the singlet spin state, while the complexes with the $CO_2^{\bullet-}$ radical were calculated in a doublet spin state. Several starting points have been considered for the orientation and the interaction site of the $CO_2^{\bullet-}$ radical on the NP, and only the most energy-stable structure is reported in the results. The electronic spectra of the systems were computed in the TD-DFT framework using the CAM-B3LYP functional and included between 600 and 1000 excited states. All the DFT calculations were performed using the ORCA 5.0.3 software[34]. The electron density generated from ORCA was analyzed by quantum chemical topological and electronic transition analyses using the Multiwfn code[35]. The analyses of both covalent and non-covalent interactions were calculated based on the Density Overlap Regions Indicator (DORI)[36]. The electron localization function (ELF) was evaluated to determine the valence basins[37].

3. Results

3.1 OD-Cu preparation and their performance in CO_2RR. The correlation of Cu(I) species with initial CO_2 activation and C–C coupling was highlighted by electrochemistry measurements[38], operando characterization[10], and DFT calculations[3]. Prior to the pulse radiolysis study, the oxide-derived Cu (OD-Cu) NPs of different oxidation states were synthesized in the homemade optical cell by an established radiolytic method[39] (See details in SI). With the known radiolytic yield (*G*-value expressed in mol/J unit) of reducing species, it is possible to control their oxidation states by varying the absorbed dose quantitatively. To avoid oxidation by air, the as-prepared samples were directly transferred to the pulse radiolysis platform without any exposure to air. The oxidation states of nanoparticles are recorded by the specific absorption bands and Cu Auger LMM XPS spectra. As shown in Figure S1, Cu LMM Auger spectra revealed the characteristic peaks corresponding to different oxidation states of Cu—Cu(I), Cu(II), and metallic Cu(0) samples, in accordance with the reported data[40-42].

To further examine the successful synthesis procedures, we initially characterize the OD-Cu NPs with electrochemical CO_2RR measurements. (Figure S2). In Cu(I) NPs, C_2H_4 was the main carbon product at low potential ranges with FE around 14% from –1.4 V to –1.1 V. The radiolytic Cu(II) NPs exhibited comparable Faraday efficiency (FE) at 10%. However, Cu(I) NPs exhibited enhanced C_2H_4 selectivity than Cu(II) NPs with a negligible FE of CO and CH_4 (<2%), while the CH_4 FE of Cu(II) was 6.5%. These electrochemical results are consistent with the previous reports[16-19] and thus represent the realization of a general synthetic strategy of OD-Cu NPs for time-resolved mechanistic study.

3.2 Kinetics of OD-Cu bound $CO_2^{\bullet-}$ radical. Figure 1b-d illustrates the key transient absorption resonance resulting from the reaction of $CO_2^{\bullet-}$ radicals with all Cu NPs from nanoseconds to submillisecond time scale:

$$\text{Cu (or OD-Cu) NP} + CO_2^{\bullet-} \rightarrow \text{Cu (or OD-Cu) NPs-}CO_2^{\bullet-}$$

The absorption band around 340 nm is attributed to surface-bound $CO_2^{\bullet-}$ on Cu(0)[43] (Figure 1e). On the surfaces of Cu(I) and Cu(II) NPs, $CO_2^{\bullet-}$ radicals exhibit more intense absorption. Notably, the peaks of Cu(I) NPs-$CO_2^{\bullet-}$ radicals (380 nm, Figure 1f) and Cu(II) NPs-$CO_2^{\bullet-}$ radicals (400 nm, Figure 1g) shift towards the visible region compared to the case of Cu(0). The negative signals at around 400 nm in Figure 1c and 450 nm in Figure 1d are due to the optical artifacts from the streak camera. Besides, Figure 1h-j shows that the formation rate can be distinguished between Cu(I) and Cu(II) NP. As a result, the spectral changes imply that the electronic structure of OD-Cu during the initial CO_2 reduction can act as the benchmark data for theoretical calculations and the experimental identification of OD-Cu-based intermediates.

The subsequent decays of surface-bound $CO_2^{\bullet-}$ radicals on Cu(0) and Cu(I) NPs exhibited second-order reactions at submillisecond timescale. Based on the concentration of Cu nanoparticles for a given size (around 9×10^{-8} mol/L) and the radiolytic yield of $CO_2^{\bullet-}$ formation (3×10^{-5} mol/L), one nanoparticle can even have hundreds of radicals adsorbed. Therefore, the probability of the surface reaction between two $CO_2^{\bullet-}$ radicals on the same nanoparticle is high. Secondly, in the case of our pulse radiolysis condition (with 5 ps pulse duration), the reverse reaction of surface adsorption is negligible, we solely observed the surface reaction. According to the Langmuir-Hinshelwood-Hougen-Watson model:

$$CO_2^{\bullet-}{}_{ad} + CO_2^{\bullet-}{}_{ad} \leftrightarrow P$$

The rate of surface reaction is given as $r = k\,(CO_2^{\bullet-}{}_{ad})^2 - k'\,(P)$. Since the reverse reaction is negligible, the overall reaction would be second order ($r = k\,(CO_2^{\bullet-}{}_{ad})^2$). However, the reaction between two nanoparticles at millisecond range is not excluded. Therefore, we propose the second order decay is

attributed to the coupling reaction of $CO_2^{\bullet-}$ radicals on the same nanoparticle or different nanoparticles. Moreover, the absorption spectra of molecular products, such as CO, formate, and oxalate, are beyond our detection limit in the UV region, so the decay can solely be attributed to radical-coupling reactions (Figure 1k-m).

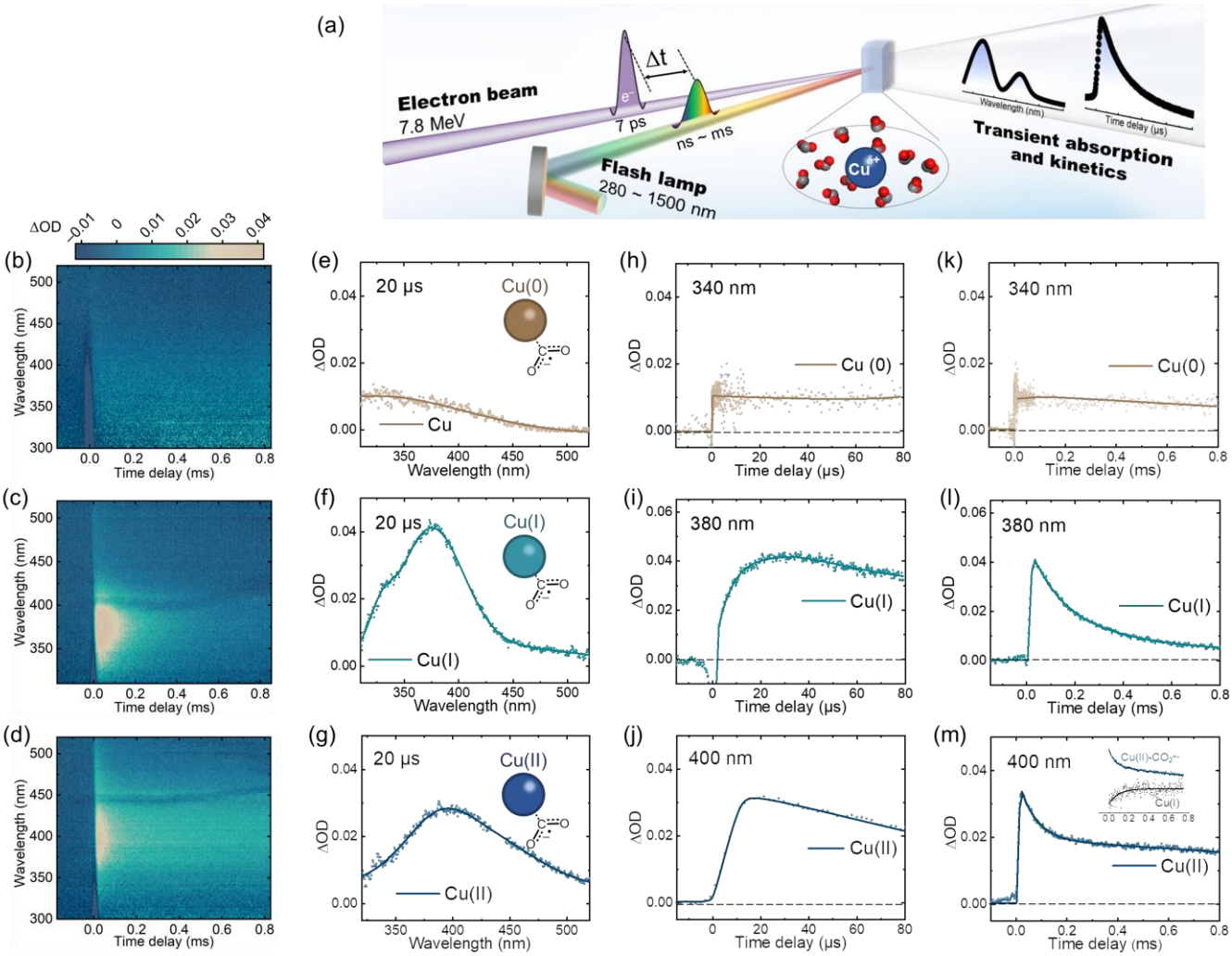

Figure 1. (a) Schematic of the experimental setup for pulse radiolysis: picosecond laser-triggered 7.8 MeV electron beam and the time-resolved absorption spectrophotometric detection system. Transient absorption matrix within 820 μs recorded by pulse radiolysis of CO_2-saturated solution containing 0.1 M formate in the presence of 0.5 mM Cu(0) (b), Cu(I) (c), Cu(II) (d) NPs. Transient absorption spectra at 20 μs for Cu(0) (e), Cu(I) (f), Cu(II) (g) NPs. Transient kinetics within 80 μs for Cu(0) NPs at 420 nm (h), Cu(I) NPs at 370 nm (i), and Cu(II) NPs at 380 nm (j). Transient kinetics within 800 μs for Cu(0) NPs at 420 nm (k), Cu(I) NPs at 370 nm (l), and Cu(II) NPs at 380 nm (m). The negative signal in Figures corresponds to the Cherenkov light. Inset: The fitting kinetics curves of the decay show the involvement of two species.

The half-time for $CO_2^{\bullet-}$ on Cu(I) (155 μs) is over 10-fold shorter than Cu(0), suggesting a faster coupling kinetics. The accelerated rate revealed that the contribution of Cu NPs' oxidation states to C–C coupling was in line with the enhanced selectivity of C_2H_4. By contrast, Cu(II) NPs-$CO_2^{\bullet-}$ displays a more complex kinetics that may involve an electron transfer reaction (Figure 1m). To clarify the elementary process, we model the transient behavior by SK-Ana software[44]. The deconvoluted data indicates the lifetime of Cu(II) NPs-$CO_2^{\bullet-}$ (Figure 1m inset) is around ms. It is known that the reaction of $CO_2^{\bullet-}$ with bulk Cu^{2+} ions occurs very fast. So, the long-lived Cu(II) NPs- $CO_2^{\bullet-}$ are uncommon and should yield distinct products. The spectral data lead us to conclude that Cu(II) surfaces typically facilitate electron transfer in $CO_2^{\bullet-}$ radicals, while Cu(I) emerges as the genuine active component for OD-Cu in the coupling reaction.

3.3 Molecular simulations of OD-Cu bound $CO_2^{\bullet-}$ radical. Molecular simulations at the DFT level were conducted to elucidate experimental absorption bands of $CO_2^{\bullet-}$ radicals interacting with different Cu nanoparticles (NPs), incorporating solvent effects through a dielectric continuum model. The calculations on the Cu(0) NP with different atoms (38 and 50) were conducted as previously reported[43] (Figure S3). The size of Cu(0) NP does not affect the general trend of the simulation results. More importantly, the nature of the interaction of $CO_2^{\bullet-}$ radicals with Cu(I) and Cu(II) NPs was investigated

(Figure 2). For Cu(II), $CO_2^{\bullet-}$ species exhibited a linear geometry as a neutral CO_2 molecule and a weak interaction with a 3.03 Å distance between the carbon atom and the nearest Cu atom. Such structure indicated that $CO_2^{\bullet-}$ radical had transferred its single electron to Cu (II) NP. The electron transition process corroborated the above transient kinetics. ELF topological analysis and DORI plot evidenced van der Waals interactions without covalency between $CO_2^{\bullet-}$ radical and Cu(II) NP.

In contrast, for Cu(I), interfacial $CO_2^{\bullet-}$ absorption occurred with a bent geometry, interacting through the O atom with a 1.92 Å distance. Partial covalency (–0.55 electrons) was aligned with a Cu-O bond with a Mayer Bond order of 0.5, and an ELF valence basin indicated the sharing of 2.03 electrons. Accounting for the loss of a few oxygen atoms in the simulation has little impact on the nature of the interaction and the electronic spectrum, keeping a bent structure of the $CO_2^{\bullet-}$ radical with a partial electron transfer (Figure S4 and Table S1).

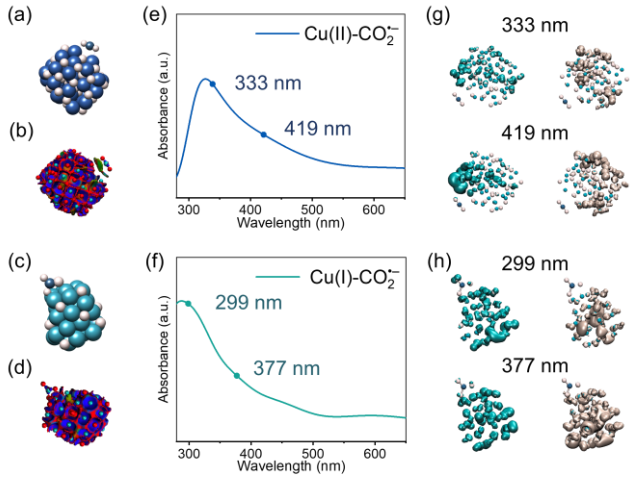

Figure 2. DFT optimized structures (a) and DORI plots(b) (repulsive forces in red and covalent interaction in blue) of Cu(II) NPs-$CO_2^{\bullet-}$. DFT optimized structures (c) and DORI plots(d) of Cu(I) NPs-$CO_2^{\bullet-}$. TD-DFT electronic spectra of Cu(II) NPs-$CO_2^{\bullet-}$ (e) and Cu(I) NPs-$CO_2^{\bullet-}$ (f). electronic transition analysis (hole in blue and electron in green) of Cu(II) NPs-$CO_2^{\bullet-}$ (g) and Cu(I) NPs-$CO_2^{\bullet-}$ (h).

These findings illustrated a significant difference in the intermolecular interaction strength between those for Cu(II) and Cu(I). TD-DFT calculations revealed the distinct absorption bands for Cu(I) and Cu(II) systems interacting with $CO_2^{\bullet-}$. The Cu(I) spectrum exhibited broadening and a band maximum at 288 nm, while the Cu(II) spectrum showed a blue shift with a maximum of 328 nm. Hole-electron formalism analysis highlighted the weak interaction between $CO_2^{\bullet-}$ and Cu(II) and a more pronounced involvement of $CO_2^{\bullet-}$ in the electronic transitions for Cu(I). These results confirmed the covalent interaction between $CO_2^{\bullet-}$ and Cu(I).

3.4 Dynamic evolution of $CO_2^{\bullet-}$ on Cu(II) NPs. In the present pulse radiolysis study, we advanced a multi-step cumulative technique. By delivering the electron pulses one by one to the system, we can precisely modulate the oxidation states of OD-Cu via reactions with known radiolytic yields of $CO_2^{\bullet-}$. This method enables successive electron transfer and thus quantifies the surface evolution of OD-Cu in a more operational CO_2 reduction process.

As an example of Cu(II) NPs, after the first electron pulse, a characteristic band of Cu(II) NPs-$CO_2^{\bullet-}$ appears at 420 nm within 20 µs (Figure 3a). Subsequently, at 750 µs, it is transformed to a Cu(I) with an absorption band below 320 nm, coinciding with the decay of Cu(II) NPs-$CO_2^{\bullet-}$ (Figure 3b). With pulse increments, the band gradually shifts from 420 nm to 380 nm (Figure 3a), resembling the band of Cu(I) NPs-$CO_2^{\bullet-}$. The reduced Cu(II) absorbance at 320 nm confirms the complete transformation of the Cu(II) NP surface into Cu(I). Furthermore, the view is supported by the steady-state UV-vis spectral characterization of spent samples taken after the pulse radiolysis measurements (Figure S5).

The multi-step pulse transient kinetics (Fig.3c and 3d) associate chemical state transition from Cu(II) to Cu(I) with surface-bound intermediates kinetics. The rising kinetics at 300 nm in the initial three pulses is primarily attributed to the Cu(I) formation. The decay at 380 nm within 200 µs clearly shows the electron transfer of surface-bound $CO_2^{\bullet-}$ radicals to Cu(II). Beyond 200 µs, the electron transfer reaction to Cu(II) is nearly completed, and Cu(I) and Cu(II) NPs-$CO_2^{\bullet-}$ co-existed (Figure 3b). After four pulses, the decay gradually transforms into a more straightforward second-order decay profile. By the tenth pulse, the half-time observed at 380 nm reaches 250 µs, following the kinetics observed for pure Cu(I) NPs solution (Figure S6). The decreasing intensity of the absorbance at 300 nm verifies the total reduction of Cu(II) surfaces (Figure 3d). This analysis reveals the dynamic evolution of Cu(II) during CO_2 reduction: initial electron transfer from $CO_2^{\bullet-}$ radicals to Cu(II) results in Cu(I) formation within 200 µs (Cu(II) NPs-$CO_2^{\bullet-}$ → $Cu(I)_{ad}$ + CO_2, where $Cu(I)_{ad}$ represents Cu(I) at the surface of Cu(II) NPs). Subsequently, the sustained decay suggests the transformation of surface-bound $CO_2^{\bullet-}$ radicals to other reduction products rather than the exclusive formation of CO_2 (Cu(II) NPs-$CO_2^{\bullet-}$ → products). As more Cu(I) sites are produced, the $CO_2^{\bullet-}$ coupling reaction on Cu(I) is favorable, with the half-time shrinking to 250 µs. Therefore, from the dynamic evolution of $CO_2^{\bullet-}$ on Cu(II) NPs, it is concluded that Cu(I) is identified as the real active site of OD-Cu for the coupling reaction, even in the presence of subsurface Cu(II).

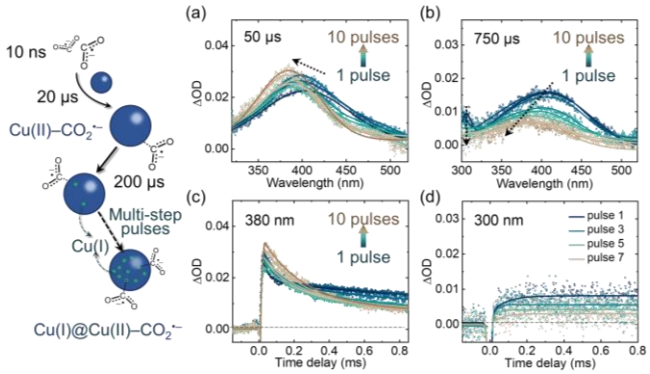

Figure 3. Transient absorption spectra as a function of the number of the electron pulse in CO_2-saturated 0.1 M formate solution in the presence of 0.5 mM Cu(II) NPs at 50 µs (a) and 750 µs (b). Transient kinetics within 820 µs as a function of the number of electron pulses at 380 nm (c) and 300 nm (d).

3.5 Dynamic evolution of $CO_2^{\bullet-}$ on Cu(I) NPs. In the context of electrochemical CO_2 reduction (eCO_2R) involving OD-Cu, one of the central debates concerns the dynamic involvement of Cu(I)[45-47]. Stabilizing the Cu(I) state in solution and decoupling it from the impact of applied external potential is chal-

lenging. In operational cases, Cu-based catalysts are mostly partially oxidized Cu(I). By utilizing pulse radiolysis experiments with or without additional electron injection, we can either couple or decouple the effect of the external potential to elucidate the dynamic evolution of Cu(I). Three partially oxidized or reduced Cu(I) NPs were synthesized as described in Scheme 1: Two variants, Cu(I)-A and Cu(I)-B, contained different amounts of Cu(II) on the surfaces. Cu(I)-C had Cu(I) NPs with Cu(0) on the surfaces for comparison. The nature of these Cu species was verified using UV-vis absorption spectra (Figure S7).

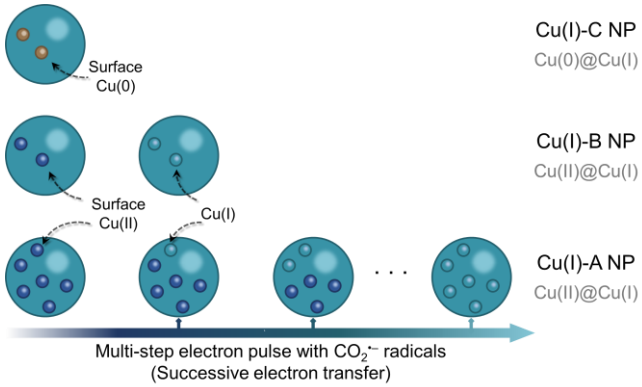

Scheme 1. OD-Cu species and their transformation by multi-step electron pulses.

Reactivity of $CO_2^{\bullet-}$ with Cu(I)-A NPs. Cu(I)-A NPs are synthesized via controllable irradiation dose (920 Gy) of a solution of Cu^{II} ions via partial reducing reactions. Then, the samples are transferred to a pulse radiolysis experiment in CO_2-saturated 0.1 M formate aqueous solutions. In this case, $CO_2^{\bullet-}$ radicals solely exist in the irradiated system induced by e_{aq}^-. $OH^\bullet$ and $H^\bullet$ were scavenged ($^\bullet OH + HCOO^- \rightarrow CO_2^{\bullet-} + H_2O$, k_2 = 4.1×10^9 M^{-1} s^{-1}; $^\bullet H + HCOO^- \rightarrow CO_2^{\bullet-} + H_2$, k_3 = 2.1×10^9 M^{-1} s^{-1})[6, 48]. Figure 4a illustrates a sequence of transient kinetics at 370 nm across a multi-step cumulative pulse. The second-order decays (Figure S8a-b) are assigned to the occurrence of $CO_2^{\bullet-}$ radicals coupling on Cu(I)-A surfaces. However, the initial absorbance intensities rise with increased electron pulses. During the first electron pulse, Cu(II) or the dissolved Cu^{II} ions from the Cu(I)-A surface is reduced to Cu(I). The signal enhancement can be attributed to $CO_2^{\bullet-}$ radicals bounded to the newly formed Cu(I) sites at the surfaces, displaying a higher extinction coefficient than Cu(II). Owing to the limited content of Cu(II) and Cu^{II} ions, we are not able to observe the signal of Cu(I) formation, but a new signal at 480 nm (Figure 4b) confirms the formation of $CuCO_2$. This occurs due to the reaction between Cu^I ions from reduced Cu^{II} and $CO_2^{\bullet-}$ radicals at 20 μs ($Cu^I + CO_2^{\bullet-} \rightarrow CuCO_2$). The rapid Cu(II) reduction is confirmed by the drop in intensity at 480 nm (Figure 4c). At the end of several pulses, Cu(I)-A NP contains almost totally Cu(I), so the decays gradually converge to that observed for neat Cu(I). With the decrease of Cu(II) sites, the faster electron transfer between Cu(II) and $CO_2^{\bullet-}$ gradually diminished and transformed to slower $CO_2^{\bullet-}$ coupling reaction on Cu(I) alone. This fact is evidenced by the extension of the half-time from 90 μs to 150 μs following two pulses, eventually stabilizing at 155 μs. After 200 μs decay, the transient absorption spectra exclusively feature surface-bound on Cu(I) NPs-$CO_2^{\bullet-}$ radicals, implying the complete reduction of the sample Cu(I)-A into Cu(I) NP (Figure 4d and Figure S8c).

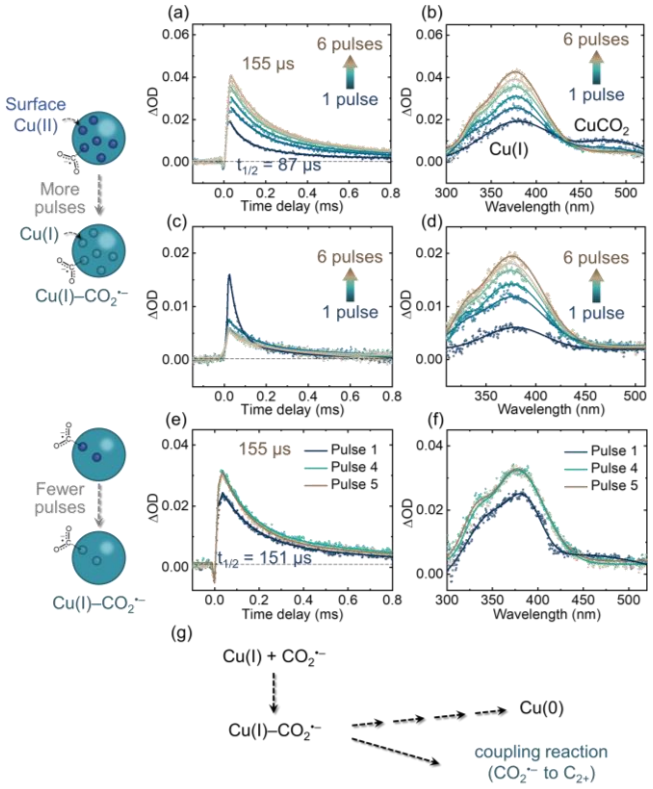

Figure 4. (a) Transient kinetics of Cu(I)-A within 800 μs as a function of pulses at 370 nm. Transient absorption spectra of Cu(I)-A as a function of pulses at 20 μs (b), transient kinetics at 480 nm (c), and Transient absorption spectra at 200 μs (d). Transient kinetics of Cu(I)-B within 800 μs as a function of pulses at 370 nm (e) and transient absorption spectra of Cu(I)-B at 20 μs (f). (g) Schematic of reaction pathway of surface-bound $CO_2^{\bullet-}$ on Cu(I).

Reactivity of $CO_2^{\bullet-}$ with Cu(I)-B NPs. For sample Cu(I)-B, the higher absorbed dose with 1.8 kGy leads to an almost full reduction during preparation. In this case, a much lower Cu(II) content is located on the surface of Cu(I) NPs. Correspondingly, the transient kinetics at 370 nm of Cu(I)-B is identical to the second-order decay of Cu(I) NPs-$CO_2^{\bullet-}$ radicals. Nevertheless, the incremental reduction for surface Cu(II) was remarkably suppressed. (Figure 3e-f). Upon the first pulse, the stronger intensity than that of Cu(I)-A suggests a higher initial concentration of Cu(I) sites available for $CO_2^{\bullet-}$ radicals. For this reason, the coupling reaction is accelerated with a half-time of 150 μs in proximity to the saturated Cu(I) state (155 μs) (Figure 3e and Figure S8d-f). Moreover, the signal for $CuCO_2$ is nearly negligible at 20 μs (Figure 3f). After 4 pulses, both the transient profiles approach those of a pure Cu(I) state with an identical rate for the coupling reaction. These comparable results showed that the different surface distributions of Cu(II) on Cu(I) nanoparticle surfaces would not influence the final reaction kinetics.

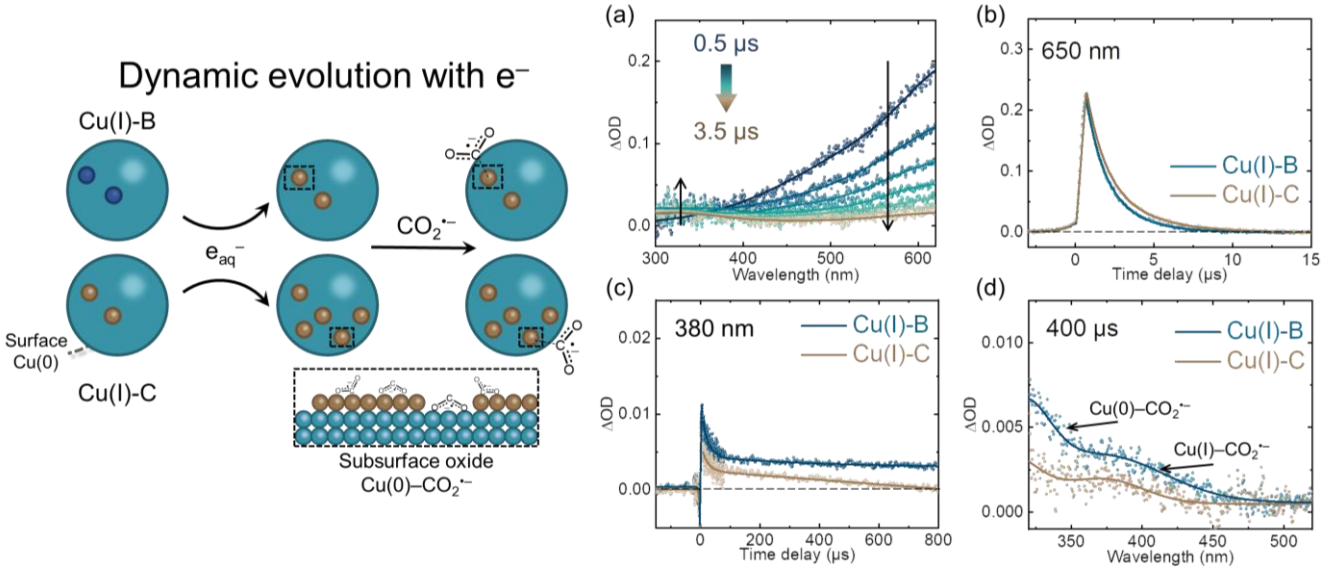

Figure 5. (a) Transient absorption spectra range from 0.5 μs to 3.5 μs of Cu(I)-B. TranSent kinetics of Cu(I)-B and Cu(I)-C at 650 nm within 15 μs (b), at 380 nm within 800 μs (c), and transient absorption spectra at 400 μs (d).

To check whether Cu(I) reduction to Cu(0) occurs, we further extended the electron-beam irradiation of Cu(I)-B (with almost pure Cu(I) form) under CO_2 reduction conditions from 1 kGy up to 12 kGy (equating to a cumulative total of 7.2 mM $CO_2^{\bullet-}$ radicals). We do not observe the obvious transition from Cu(I) to Cu(0). The transient kinetics only exhibited typical second-order kinetics of Cu(I)-$CO_2^{\bullet-}$ radicals and a sluggish decrease in the initial intensity (Figure S9). On the one hand, this kinetics can be attributed to the redox potential of $CO_2^{\bullet-}$ radicals (–2.0 eV) compared to Cu(I) (between – 2.6 eV for Cu^I/Cu_{atom} to – 0.36 eV for Cu^I/Cu_{metal})[24, 49]. On the other hand, insight from recent large-scale molecular dynamics simulations revealed that the reduction dynamics of Cu(I) necessitated a considerable amount of time to remove all the trapped oxygen and to reconstruct Cu surfaces[50].

These observations underscored critical evidence in the case of CO_2 reduction under pH conditions of 7.8 with 5 nm Cu catalysts in different oxidation states: during the CO_2 reduction, Cu(I) predominately stabilizes $CO_2^{\bullet-}$ radicals for further coupling reaction rather than being reduced to Cu(0). Specifically, the partially oxidized surface of Cu(I) primarily loses a segment of $CO_2^{\bullet-}$ radicals to complete the reduction of oxidized Cu(I). Still, the presence of a small amount of Cu(II) accelerates the radical coupling reaction. Once the Cu(I) state is fully formed, the coupling reaction rate is maintained, independent of the initial surface oxidation state. Based on the redox potential of Cu(I), our time-resolved results shed new sights into the elementary CO_2RR process, especially under applied potential above –0.36 eV.

To simulate the operational conditions at lower applied potential, we investigate the dynamic evolution of Cu(I)-B NP with electron injection. In the Ar-saturated solution, two reducing radicals (e_{aq}^- and $CO_2^{\bullet-}$ radicals) are simultaneously produced by electron pulse. The distinct transient absorption profile of each species was observed (Figure 5a). An intense broad absorption band of e_{aq}^- appears within 0.5 μs and gradually diminishes (Figure 5b). The observation shows that e_{aq}^- can reduce Cu(I) to Cu(0). The formation of Cu(0) species is identified by the irradiated samples after pulse radiolysis (Figure S10). A new absorption band for surface-bound $CO_2^{\bullet-}$ radicals on both Cu(0) and Cu(I) are observed (Figure 5c-d). Cu(I)-$CO_2^{\bullet-}$ radicals decayed much faster than on Cu(0)-$CO_2^{\bullet-}$ (Figure 1g and 1h), so a higher intensity appeared at 320 nm than at 380 nm (Figure 5d). These results revealed that once the decay of e_{aq}^- was complete, $CO_2^{\bullet-}$ radicals were adsorbed onto Cu(I) and Cu(0) with subsurface oxide.

Reactivity of $CO_2^{\bullet-}$ with Cu(I)-C NPs. Recent studies provide the insight that subsurface oxide plays a critical role in the initial steps for activating CO_2. The subsurface oxide structure would promote H_2O chemisorption onto the Cu^+ center. This enables the electronic communication between adsorbed CO_2 and H_2O, favoring the transition from a linearly physisorbed CO_2 to $CO_2^{\bullet-}$ radicals. To underline the potential role of subsurface oxide[2, 51], we prepared Cu(I) NPs incorporating Cu(0) as a reference by irradiation at 4 kGy (Cu(I)-C). As discussed above, the surface reduction of Cu(I) to transient Cu(0) with subsurface oxide was achieved within 10 μs. In comparison with Cu(I)-B, Cu(I)-C surfaces had a portion of Cu(I) sites replaced by Cu(0), with a lower density of subsurface oxide. Comparative analysis of Cu(I)-C and Cu(I)-B reveals distinct kinetics at 380 nm (Figure 5c). Both Cu(I)-B and Cu(I)-C show a similar decay for the first 50 μs. However, Cu(I)-B presents slower decay and higher intensity later due to the more subsurface oxide sites on its surface than Cu(I)-C. Such difference in transient dynamics strongly supports the notion that subsurface oxide plays a constructive role in stabilizing $CO_2^{\bullet-}$ radicals at the surface. Notably, the red-shift observed in the transient absorption spectra of Cu(I)-B relative to Cu(I)-C further emphasizes the manifestation of a more delocalized interaction involving $CO_2^{\bullet-}$ radicals (Figure 5d). The interaction enhanced the activation propensity of $CO_2^{\bullet-}$ radicals and facilitated their engagement in subsequent reactions.

4. CONCLUSIONS

In summary, our study integrated nanoscale OD-Cu manipulation with pulse radiolysis to unravel the intricate role of copper oxidation states on the interfacial dynamics of $CO_2^{\bullet-}$ intermediate. Pulse radiolysis measurements, combined with molecular simulations, dictated the benchmark data for the formation and decay of surface-bound $CO_2^{\bullet-}$ radicals on vari-

ous OD-Cu. Cu(II) surfaces dominate electron transfer from $CO_2^{\bullet-}$ radicals to form Cu(I) within 200 μs, while Cu(I) emerges as the genuine active site for OD-Cu in the coupling reaction and stabilizes $CO_2^{\bullet-}$ radicals for a considerably longer time without electron transfer. The multi-step methodology quantitatively captured the dynamic evolution of OD-Cu with different oxidation states. The beneficial role of subsurface oxide in the initial adsorption and activation of $CO_2^{\bullet-}$ radicals was also verified. This study of monitoring the transient kinetics of interfacial intermediates establishes a foundational experimental methodology for elucidating heterogeneous catalysis mechanisms from an elementary reaction perspective.

ASSOCIATED CONTENT

The Supporting Information is available free of charge via the Internet at http://pubs.acs.org.

Steady-state UV-vis absorption spectra of different Cu species, Faraday efficiency analysis, and transient absorption and fitting curves for transient kinetics of intermediates.

AUTHOR INFORMATION

Corresponding Author

*majun0502@ustc.edu.cn; mehran.mostafavi@universite-paris-saclay.fr

Notes

The authors declare no competing financial interest.

ACKNOWLEDGMENT

This work was supported by the National Natural Science Foundation of China (11975122, 22006067, and 21906083), Jiangsu Province Science Fund for Distinguished Young Scholars (BK20230032), Fundamental Research Funds for the Central Universities (NE2020006), Scientific and Technological Innovation Special Fund for Carbon Peak and Carbon Neutrality of Jiangsu Province (BK20220026), and Postdoctoral Fellowship Program of CPSF (GZC20232529). We thank Jean-Philippe Larbre for his help during the experiments at ELYSE and Dr. Feng Hu of NUAA for their kind help with the electrochemical analysis.

REFERENCES

1. Cheng, D.; Zhao, Z.; Zhang, G.; Yang, P.; Li, L.; Gao, H.; Liu, S.; Chang, X.; Chen, S.; Wang, T.; Ozin, G. A.; Liu, Z.; Gong, J. The nature of active sites for carbon dioxide electroreduction over oxide-derived copper catalysts. *Nat. Commun.* **2021**, *12*, 395. DOI: 10.1038/s41467-020-20615-0.

2. Favaro, M.; Xiao, H.; Cheng, T.; Goddard, W. A.; Crumlin, E. J. Subsurface oxide plays a critical role in CO_2 activation by Cu(111) surfaces to form chemisorbed CO_2, the first step in reduction of CO_2. *Proc. Natl. Acad. Sci. USA* **2017**, *114,* 6706–6711. DOI: 10.1073/pnas.1701405114.

3. Li, H.; Jiang, Y.; Li, X.; Davey, K.; Zheng, Y.; Jiao, Y.; Qiao, S. C_{2+} selectivity for CO_2 electroreduction on oxidized Cu-based catalysts. *J. Am. Chem. Soc.* **2023**, *145*, 14335–14344. DOI: 10.1021/jacs.3c03022.

4. Mistry, H.; Varela, A. S.; Bonifacio, C. S.; Zegkinoglou, I.; Sinev, I.; Choi, Y.; Kisslinger, K.; Stach, E. A.; Yang, J. C.; Strasser, P.; Cuenya, B. R. Highly selective plasma-activated copper catalysts for carbon dioxide reduction to ethylene. *Nat. Commun.* **2016**, *7,* 12123. DOI: 10.1038/ncomms12123.

5. Liu, G.; Zhang, F.; Li, J.; Zeng, G.; Ye, Y.; Larson, D. M.; Yano, J.; Crumlin, E. J.; Ager, J. W.; Wang, L.; Toma, F. M. Investigation and mitigation of degradation mechanisms in Cu_2O photoelectrodes for CO_2 reduction to ethylene. *Nat. Energy* **2021**, *6,* 1124–1132. DOI: 10.1038/s41560-021-00927-1.

6. Hu, C.; Jiang, Z.; Wu, Q.; Cao, S.; Li, Q.; Chen, C.; Yuan, L.; Wang, Y.; Yang, W.; Yang, J.; Peng, J.; Shi, W.; Zhai, M.; Mostafavi, M.; Ma, J. Selective CO_2 reduction to CH_3OH over atomic dual-metal sites embedded in a metal-organic framework with high-energy radiation. *Nat. Commun.* **2023**, *14,* 4767. DOI: 10.1038/s41467-023-40418-3.

7. Lai, W.; Ma, Z.; Zhang, J.; Yuan, Y.; Qiao, Y.; Huang, H. Dynamic evolution of active sites in electrocatalytic CO_2 reduction reaction: fundamental understanding and recent progress. *Adv. Funct. Mater.* **2022**, *32,* 2111193. DOI: 10.1002/adfm.202111193.

8. Wang, J.; Chen, H.; Tan, H.; Tan, C. M.; Zhu, Y.; Chen, H. M. Strong correlation between the dynamic chemical state and product profile of carbon dioxide electroreduction. *ACS Appl. Mater. Interfaces* **2022**, *14,* 22681–22696. DOI: 10.1021/acsami.1c19380.

9. Vavra, J.; Shen, T. H.; Stoian, D.; Tileli, V.; Buonsanti, R. Real-time monitoring reveals dissolution/redeposition mechanism in copper nanocatalysts during the initial stages of the CO_2 reduction reaction. *Angew. Chem. Int. Ed.* **2021**, *60,* 1347–1354. DOI: 10.1002/anie.202011137.

10. Yang, Y.; Louisia, S.; Yu, S.; Jin, J.; Roh, I.; Chen, C.; Guzman, M. V. F.; Feijóo, J.; Chen, P.; Wang, H.; Pollock, C. J.; Huang, X.; Shao, Y.; Wang, C.; Muller, D. A.; Abruña, H. D.; Yang, P. Operando studies reveal active Cu nanograins for CO_2 electroreduction. *Nature* **2023**, *614,* 262–269. DOI: 10.1038/s41586-022-05540-0.

11. Handoko, A. D.; Wei, F.; Jenndy; Yeo, B. S.; Seh, Z. W. Understanding heterogeneous electrocatalytic carbon dioxide reduction through operando techniques. *Nat. Catal.* **2018**, *1,* 922–934. DOI: 10.1038/s41929-018-0182-6.

12. Dattila, F.; García-Muelas, R.; López, N. Active and selective ensembles in oxide-derived copper catalysts for CO_2 reduction. *ACS Energy Lett.* **2020**, *5*, 3176–3184. DOI: 10.1021/acsenergylett.0c01777.

13. Li, Y.; Ozden, A.; Leow, W. R.; Ou, P.; Huang, J. E.; Wang, Y.; Bertens, K.; Xu, Y.; Liu, Y.; Roy, C.; Jiang, H.; Sinton, D.; Li, C.; Sargent, E. H. Redox-mediated electrosynthesis of ethylene oxide from CO_2 and water. *Nat. Catal.* **2022**, *5,* 185–192. DOI: 10.1038/s41929-022-00749-8.

14. Kim, Y. G.; Baricuatro, J. H.; Javier, A.; Gregoire, J. M.; Soriaga, M. P. The evolution of the polycrystalline copper surface, first to Cu(111) and then to Cu(100), at a fixed CO_2RR potential: a study by operando EC-STM. *Langmuir* **2014**, *30*, 15053–15056. DOI: 10.1021/la504445g.

15. Han, Z.; Han, D.; Chen, Z.; Gao, J.; Jiang, G.; Wang, X.; Lyu, S.; Guo, Y.; Geng, C.; Yin, L.; Wang, Z.; Yang, Q. H. Steering surface reconstruction of copper with electrolyte additives for CO_2 electroreduction. *Nat. Commun.* **2022**, *13*, 3158. DOI: 10.1038/s41467-022-30819-1.

16. Eilert, A.; Roberts, F. S.; Friebel, D.; Nilsson, A. Formation of copper catalysts for CO_2 reduction with high ethylene/methane product ratio investigated with in situ X-ray absorption spectroscopy. *J. Phys. Chem. Lett.* **2016**, *7*, 1466–1470. DOI: 10.1021/acs.jpclett.6b00367.

17. Scholten, F.; Sinev, I.; Bernal, M.; Cuenya, B. R. Plasma-modified dendritic Cu catalyst for CO_2 electroreduction. *ACS Catal.* **2019**, *9*, 5496–5502. DOI: 10.1021/acscatal.9b00483.

18. Gao, D.; Zegkinoglou, I.; Divins, N. J.; Scholten, F.; Sinev, I.; Grosse, P.; Cuenya, B. R. Plasma-activated copper nanocube catalysts for efficient carbon dioxide electroreduction to hydrocarbons and alcohols. *ACS Nano* **2017**, *11*, 4825–4831. DOI: 10.1021/acsnano.7b01257.

19. Jung, H.; Lee, S. Y.; Lee, C. W.; Cho, M. K.; Won, D. H.; Kim, C.; Oh, H. S.; Min, B. K.; Hwang, Y. J. Electrochemical fragmentation of Cu_2O nanoparticles enhancing selective C-C coupling from CO_2 reduction reaction. *J. Am. Chem. Soc.* **2019**, *141*, 4624–4633. DOI: 10.1021/jacs.8b11237.

20. Lee, S. H.; Lin, J. C.; Farmand, M.; Landers, A. T.; Feaster, J. T.; Avilés Acosta, J. E.; Beeman, J. W.; Ye, Y.; Yano, J.; Mehta, A.;

Davis, R. C.; Jaramillo, T. F.; Hahn, C.; Drisdell, W. S. Oxidation state and surface reconstruction of Cu under CO_2 reduction conditions from in situ X-ray characterization. *J. Am. Chem. Soc.* **2021**, *143*, 588–592. DOI: 10.1021/jacs.0c10017.

21. Balcerzyk, A.; Schmidhammer, U.; Horne, G.; Wang, F.; Ma, J.; Pimblott, S. M.; de la Lande, A.; Mostafavi, M. Unexpected ultrafast silver ion reduction: dynamics driven by the solvent structure. *J. Phys. Chem. B* **2015**, *119*, 10096–10101. DOI: 10.1021/acs.jpcb.5b04907.

22. Wang, F.; Archirel, P.; Muroya, Y.; Yamashita, S.; Pernot, P.; Yin, C.; El Omar, A. K.; Schmidhammer, U.; Teuler, J. M.; Mostafavi, M. Effect of the solvation state of electron in dissociative electron attachment reaction in aqueous solutions. *Phys. Chem. Chem. Phys.* **2017**, **19**, 23068–23077. DOI: 10.1039/C7CP03997B.

23. Ma, J.; Schmidhammer, U.; Pernot, P.; Mostafavi, M. Reactivity of the strongest oxidizing species in aqueous solutions: The short-lived radical cation $H_2O^{\bullet+}$. *J. Phys. Chem. Lett.* **2014**, *5*, 258–261. DOI: 10.1021/jz402411x.

24. Khatouri, J.; Mostafavi, M.; Amblard, J.; Belloni, J. Radiation-induced copper aggregates and oligomers. *Chem. Phys. Lett.* **1992**, *191*, 351–356. DOI: 10.1016/0009-2614(92)85313-Y.

25. Belloni, J.; Marignier, J. L.; Mostafavi, M. Mechanisms of metal nanoparticles nucleation and growth studied by radiolysis. *Radiat. Phys. Chem.* **2020**, *169*, 107952. DOI: 10.1016/j.radphyschem.2018.08.001.

26. Shcherbakov, V.; Denisov, S. A.; Mostafavi, M. The mechanism of organic radical oxidation catalysed by gold nanoparticles. *Phys. Chem. Chem. Phys.* **2021**, *23*, 26494–26500. DOI: 10.1039/D1CP03875C.

27. Hu, C.; AI Gharib, S.; Wang, Y.; Gan, P.; Li, Q.; Denisov, S. A.; Le Caer, S.; Belloni, J.; Ma, J.; Mostafavi, M. Radiolytic approach for efficient, selective and catalyst-free CO_2 conversion at room temperature. *ChemPhysChem* **2021**, *22*, 1900–1906. DOI: 10.1002/cphc.202100378.

28. Ren, H.; Kovalev, M.; Weng, Z.; Muhamad, M. Z.; Ma, H.; Sheng, Y.; Sun, L.; Wang, J.; Rihm, S.; Yang, W.; Lapkin, A. A.; Ager, J. W. Operando proton-transfer-reaction time-of-flight mass spectrometry of carbon dioxide reduction electrocatalysis. *Nat. Catal.* **2022**, *5*, 1169–1179. DOI: 10.1038/s41929-022-00891-3.

29. Sheng, H.; Oh, M. H.; Osowiecki, W. T.; Kim, W.; Alivisatos, A. P.; Frei, H. Carbon Dioxide dimer radical anion as surface intermediate of photoinduced CO_2 reduction at aqueous Cu and CdSe nanoparticle catalysts by rapid-Scan FT-IR spectroscopy. *J. Am. Chem. Soc.* **2018**, *140*, 4363–4371. DOI: 10.1021/jacs.8b00271.

30. Zhang, H.; Xu, C.; Zhan, X.; Yu, Y.; Zhang, K.; Luo, Q.; Gao, S.; Yang, J.; Xie, Y. Mechanistic insights into CO_2 conversion chemistry of copper bis-(terpyridine) molecular electrocatalyst using accessible operando spectrochemistry. *Nat. Commun.* **2022**, *13*, 6029. DOI: 10.1038/s41467-022-33689-9.

31. Grimme, S.; Ehrlich, S.; Goerigk, L. Effect of the damping function in dispersion corrected density functional theory. *J. Comput. Chem.* **2011**, *32*, 1456-1465. DOI: 10.1002/jcc.21759.

32. Gontrani, L.; Bauer, E. M.; Talone, A.; Missori, M.; Imperatori, P.; Tagliatesta, P.; Carbone, M. CuO Nanoparticles and Microaggregates: An Experimental and Computational Study of Structure and Electronic Properties. *Materials*, **2023**, *16*(13), 4800. DOI: 10.3390/ma16134800.

33. Neuburger, M. C. Präzisionsmessung der Gitterkonstante von Cuprooxyd Cu_2O. Zeitschrift für Physik, **1931**, *67*, 845–850. DOI: 10.1007/BF01390765.

34. Neese, F. The ORCA program system. *Wiley Interdiscip. Rev. Comput. Mol. Sci.* **2012**, *2*, 73–78. DOI: 10.1002/wcms.81.

35. Lu, T.; Chen, F. Multiwfn: a multifunctional wavefunction analyzer. *J. Comput. Chem.* **2012**, *33*, 580–592. DOI: 10.1002/jcc.22885.

36. Silva, P. De. Simultaneous visualization of covalent and noncovalent interactions using regions of density overlap. *J. Chem. Theory Comput.* **2014**, *10*, 3745-3756. DOI: 10.1021/ct500490b.

37. Becke, A. D.; Edgecombe, K. E. A simple measure of electron localization in atomic and molecular systems. *J. Chem. Phys.* **1990**, *92*, 5397–5403. DOI: 10.1063/1.458517.

38. Timoshenko, J.; Bergmann, A.; Rettenmaier, C.; Herzog, A.; Arán-Ais, R. M.; Jeon, H. S.; Haase, F. T.; Hejral, U.; Grosse, P.; Kühl, S.; Davis, E. M.; Tian, J.; Magnussen, O.; Cuenya, B. R. Steering the structure and selectivity of CO_2 electroreduction catalysts by potential pulses. *Nat. Catal.* **2022**, *5*, 259–267. DOI: 10.1038/s41929-022-00760-z.

39. Kecht, J.; Tahri, Z.; De Waele, V.; Mostafavi, M.; Mintova, S.; Bein, T. Colloidal zeolites as host matrix for copper nanoclusters. *Chem. Mater.* **2006**, *18*, 3373-3380. DOI: 10.1021/cm052312c.

40. Borgohain, K.; Murase, N.; Mahamuni, S. Synthesis and properties of Cu_2O quantum particles. *J. Appl. Phys.* **2002**, *92*, 1292–1297. DOI: 10.1063/1.1491020.

41. Yin, M.; Wu, C. K.; Lou, Y.; Burda, C.; Koberstein, J. T.; Zhu, Y.; O'Brien, S. Copper oxide nanocrystals. *J. Am. Chem. Soc.* **2005**, *127*, 9506–9511. DOI: 10.1021/ja050006u.

42. Arán-Ais, R. M.; Scholten, F.; Kunze, S.; Rizo, R.; Cuenya, B. R. The role of in situ generated morphological motifs and Cu(I) species in C_{2+} product selectivity during CO_2 pulsed electroreduction. *Nat. Energy* **2020**, *5*, 317–325. DOI: 10.1038/s41560-020-0594-9.

43. Jiang, Z.; Clavaguéra, C.; Hu, C.; Denisov, S. A.; Shen, S.; Hu, F.; Ma, J.; Mostafavi, M. Direct time-resolved observation of surface-bound carbon dioxide radical anions on metallic nanocatalysts. *Nat. Commun.* **2023**, *14*, 7116. DOI: 10.1038/s41467-023-42936-6.

44. Ruckebusch, C.; Sliwa, M.; Pernot, P.; de Juan, A.; Tauler, R. Comprehensive data analysis of femtosecond transient absorption spectra: A review. *J. Photochem. Photobiol. C: Photochem. Rev.* **2012**, *13*, 1-27. DOI: 10.1016/j.jphotochemrev.2011.10.002.

45. Li, C. W.; Kanan, M. W. CO_2 reduction at low overpotential on Cu electrodes resulting from the reduction of thick Cu_2O films. *J. Am. Chem. Soc.* **2012**, *134*, 7231–7234. DOI: 10.1021/ja3010978.

46. Chou, T. C.; Chang, C. C.; Yu, H. L.; Yu, W. Y.; Dong, C. L.; Velasco-Vélez, J. J.; Chuang, C. H.; Chen, L. C.; Lee, J. F.; Chen, J. M.; Wu, H. L. Controlling the oxidation state of the Cu electrode and reaction intermediates for electrochemical CO_2 reduction to ethylene. *J. Am. Chem. Soc.* **2020**, *142*, 2857–2867. DOI: 10.1021/jacs.9b11126.

47. Kim, J.; Choi, W.; Park, J. W.; Kim, C.; Kim, M.; Song, H. Branched copper oxide nanoparticles induce highly selective ethylene production by electrochemical carbon dioxide reduction. *J. Am. Chem. Soc.* **2019**, *141*, 6986–6994. DOI: 10.1021/jacs.9b00911.

48. Jiang, Z.; Yu, M.; Cao, S.; Li, M.; Liu, Y.; Wang, Y.; Zhang, Z.; Guo, W.; Ma, J. Durable oxidation-resistance of copper via light-powered bidentate binding of carbon dioxide anion radicals. *ACS Mater. Lett.* **2022**, *4*, 1967–1975. DOI: 10.1021/acsmaterialslett.2c00624.

49. Henglein, A. The reactivity of silver atoms in aqueous solutions (a γ-radiolysis study). *Bunsenges. Phys. Chem.* **1977**, *81*, 556–561. DOI: 10.1002/bbpc.19770810604.

50. Lian, Z.; Dattila, F.; López, N. Stability and lifetime of diffusion-trapped oxygen in oxide-derived copper CO_2 reduction electrocatalysts. *Nat. Catal.* **2024**, *7*, 401–411. DOI: 10.1038/s41929-024-01132-5.

51. Eilert, A.; Cavalca, F.; Roberts, F. S.; Osterwalder, J.; Liu, C.; Favaro, M.; Crumlin, E. J.; Ogasawara, H.; Friebel, D.; Pettersson, L. G. M.; Nilsson, A. Subsurface oxygen in oxide-derived copper electrocatalysts for carbon dioxide reduction. *J. Phys. Chem. Lett.* **2017**, *8*, 285–290. DOI: 10.1021/acs.jpclett.6b02273.

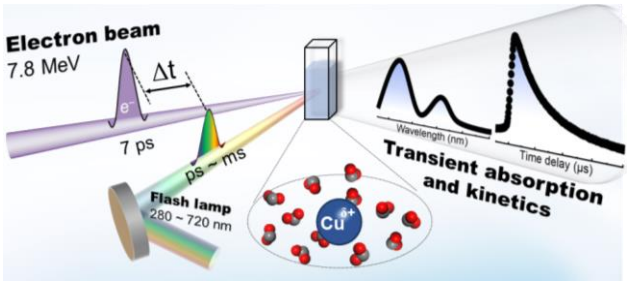

Insert Table of Contents artwork here